Nanotechnology Perceptions
ISSN 1660-6795
www.nano-ntp.com

Investigation On The Structure And Photoluminescence Properties Of PVP Capped $Mgal_2o_4:Tb^{3+}$ Doped Nanophosphors

Deepa Rani S[1,*], Carol vincent[2], Sajan P. Shamsudeen[3], and Abhilash Kumar R G [4]

[1,2]Department of Physics, Government College for Women, Thiruvananthapuram, Kerala, India – 695 014
[3]Department of Physics, University College, Thiruvananthapuram, Kerala, India – 695 034
[4]Government Arts and Science College, Ambalapuzha, Alappuzha, Kerala, India – 688 561
**Corresponding author. Email: deeparanis1970@gmail.com*

The demand for highly luminescent nanophosphors for high resolution displays and lighting with high energy saving capability are potentially important due to their numerous advantageous properties such as long lifetime, high energy efficiency, better quantum yield, better reliability and environmentally friendly characteristics. Rare earth incorporated nanophosphors have opened up exciting avenues for new applications across various fields. Spinel oxides with general formula, AB_2O_4 are indeed known for their thermal and chemical stability. Magnesium aluminate ($MgAl_2O_4$) is a well known spinel material that has been extensively used as the host material for developing phosphors due to their range of excellent properties such as low density, high melting point, good resistance against chemical attacks and excellent strength at high temperatures. In the present study, green light emitting $Mg_{1-x}Tb_xAl_2O_4$ (x = 0.02, 0.04, 0.06, 0.08 and 0.10) nanophosphors have been synthesized by polyvinylpyrrolidone *(PVP) polymer capped citrate nitrate sol-gel method. The effect of Tb^{3+} doping on the structural and luminescent characteristics of the prepared nanophosphors were examined using a variety of characterization techniques such as X- ray diffraction (XRD), Transmission electron microscopy (TEM), Fourier transform infrared spectroscopy (FTIR), UV-diffuse reflectance (DRS) and Photoluminescence (PL) spectroscopy. X-ray diffraction and transmission electron microscopic techniques reveal the structural characteristics of the prepared samples. UV visible diffuse reflectance spectra were employed to find the optical band gap of the samples by utilising the Kubelka-Munk function. Fourier transform infrared spectra provided information about various functional groups present in the samples. Photoluminescence excitation and emission spectra as well as lifetime measurements were used to analyse the luminescence dynamics of the prepared nanophosphors. Photoluminescence emission spectra comprised of two regions, characteristic of blue emissions and green emissions corresponding to $^5D_3 \rightarrow {}^7F_{J\ (J=5,\ 4,\ 3)}$ transitions and $^5D_4 \rightarrow {}^7F_{J\ (J=6,\ 5,\ 4,\ 3)}$ transitions respectively. Increase in the Tb^{3+} ion concentration lead to concentration quenching phenomenon which can be interpreted by evaluating the critical distance between the dopant ions and confirmed that phonon-assisted multipole-multipole interaction is the mechanism behind energy transfer process. Dexter's theory further concluded that the interaction involved among Tb^{3+} ions is dipole-dipole in nature.*

Evaluation of photometric parameters such as CIE co-ordinates, correlated colour temperature and colour purity indicates that the obtained phosphors can serve as promising materials for solid state lighting as well as for optoelectronic applications specifically for white LEDs.

1.Introduction

Luminescent materials have become essential to our modern society and the luminescence field has attained tremendous progress through advances in material synthesis, new spectroscopic techniques to study their properties and the need to fulfil the requirements of novel technologies. Luminescent materials dominate lighting and display applications, trendy research areas such as bio-imaging, bio-sensing, optical thermometry, photonics, information storage and in various fields of persistent light emissions [1] .One example of materials with persistent luminescence phenomenon is rare earth doped inorganic nanophosphors which are technologically important due to their sharp emission features. Trivalent rare earth ions control the duration and intensity of persistent luminescence. Substantial persistent luminescence from rare earth ions is achieved by exciting the electrons to the 5d state through irradiation with UV photons, when they are incorporated into appropriate host materials. The efficiency of nanophosphors depends on the host material, concentration and the occupancy of activators and the energy transfer efficiency of activator ions [2,3] .

In the present work, spinel type inorganic oxide magnesium aluminate ($MgAl_2O_4$) is chosen as the host material due to its desirable properties such as wide band gap, lack of radioactive elements, high tolerance to chemical attacks, high hardness, relatively low density, high electrical resistivity and excellent dielectric and optical performances [4,5] .Among the rare earth ions terbium is one of the most widely used one which emits strongly in the green region upon excitation with UV radiations [6,7] . A series of$Mg_{1-x}Tb_xAl_2O_4$ (x = 0.02, 0.04, 0.06, 0.08 and 0.10) nanophosphors have been synthesized by the polyvinylpyrrolidone (PVP) polymer capped citrate nitrate sol-gel method. PVP modifies the nanoparticles surface by acting as a capping agent, improves the surface stability and has significant influence on the morphology and optical properties of nanoparticles [8,9]. The influence of Tb^{3+} doping on the structure, morphology, optical and vibrational properties of synthesized $Mg_{1-x}Tb_xAl_2O_4$ (x = 0.02, 0.04, 0.06, 0.08 and 0.10) nanophosphors were investigated systematically.

Key words: Magnesium aluminate; Sol-gel processes; Nanoparticles; Optical properties; Photoluminescence

2.Materials and methods

The starting materials used in the synthesis were analytical grade magnesium nitrate hexahydrate ($Mg(NO_3)_2 .6H_2O$), terbium nitrate hexahydrate ($Tb(NO_3)_3.6H_2O$), aluminium nitrate nonahydrate ($Al(NO_3)_3.9H_2O$), citric acid ($C_6H_8O_7$) and polyvinylpyrrolidone ((C_6H_9NO)n, 40000 g/mol). Appropriate amounts of magnesium nitrate, aluminium nitrate and terbium nitrate were dissolved in deionized water and stirred for 1 hour a magnetic stirrer. The metal nitrate to citric acid ratio was maintained as 1:1. To this nitrate solution, citric acid was added dropwise to initiate the formation of a metal-citrate complex. To this mixture, 1 wt% PVP solution was added and stirred continuously for 3 hours to form a homogeneous polymerised precursor. The resultant solution was then kept in a hot air oven at 160 ^{O}C for 24

hours to produce a yellowish polymerised dried gel. The obtained dried powder was then finely ground and calcined in a muffle furnace at 900^{O}C for 3hours to obtain $MgAl_2O_4$:Tb^{3+} nanophosphors. X-ray diffraction measurements were done on a Bruker (D8 ADVANCE DAVINCI) X-ray diffractometer using CuKα radiation (1.54056 Å) in the angular range (2θ) from 10^{O}to 80^{O}. Microscopic structural analysis was performed using a JEOL/JEM-2100, 200 kV analytical electron microscope. Diffuse reflectance spectra were carried out on a UV-Visible NIR spectrophotometer (JASCO V-750) with $BaSO_4$ as the reference. Fourier transform infrared spectra (FTIR) were monitored by a Fourier Transform Infrared (FTIR) Spectrometer (Perkin Elmer Spectrum Two FT-IR Spectrometer) employing KBr pellet method in the wave number range of 400-4000 cm^{-1}. The excitation and emission spectra were recorded using a HORIBA SCIENTIFIC FLUOROLOG 3 spectroflurometer using 450 W Xenon lamp as the excitation source. Decay measurements were carried out in the same instrument using a phosphorimeter attachment employing a microsecond pulsed xenon lamp as the excitation source.

3. Results and Discussion

3.1. Crystal structure and morphology studies

X-ray diffraction patterns were utilised to investigate the crystal structure and phase formation of the synthesized nanophosphors.X-ray diffraction profiles of $Mg_{1-x}Tb_xAl_2O_4$ (x = 0.02, 0.04, 0.06, 0.08 and 0.10) nanophosphors (Fig.1) show well-defined peaks characteristic of the pure spinel phase. The absence of impurity peaks indicates the formation of samples with high crystalline nature, and the peaks can be indexed to the ICDD File No. 01-070-5187, with space group Fd-3m (227) cubic system.It was observed that with an increase in Tb^{3+} ion concentration, broadening of peaks occurred,which can be attributed to the reduction in the crystallite size. The diffraction pattern clearly demonstrates the successful incorporation of Tb^{3+} ion in the $MgAl_2O_4$ host lattice [10]. Debye-Scherrer formula was utilized to evaluate the crystallite size of the prepared nanophosphors, given by

$$\text{Crystallite size, D} = \frac{k\lambda}{\beta_{hkl}\cos\theta_{hkl}} \quad (1)$$

where D represents crystallite size along (hkl) direction, K is a dimensionless shape factor (= 0.99), λ is the wavelength of X-ray radiation (=1.54056 Å), β_{hkl} is the full width at half maximum and θ is the Bragg angle [11,12] . From the XRD pattern, lattice parameter (a) of the prepared phosphors was determined using the equation of cubic system, given by

$$\frac{1}{d^2} = \frac{(h^2+k^2+l^2)}{a^2} \quad (2)$$

where d represents interplanar spacing and h, k, and l, the miller indices of the corresponding plane. Expansion in lattice cell volume occurred with increase in Tb^{3+} ion concentration, which was attributed to the creation of negative pressure due to the crystallite size reduction [13]. PVP added during synthesis controlled the size of the nanoparticles obtained, by acting as a capping agent [14]. Variation of lattice parameter, crystallite size and cell volume of the synthesized phosphors as a function of Tb^{3+} ion concentration is shown in (Fig. 2).

Transmission electron microscopic image of $Mg_{0.96}Tb_{0.04}Al_2O_4$ (Fig.3) illustrates the formation of spherically morphological particles with well defined grain boundaries and slight agglomerations.The results confirmed the formation of a perfect crystalline sample with particle size of about 12 nm, which agrees well with the result obtained from Debye-Scherrer formula.Hence, PVP acted as a stabilising agent, prevented agglomeration and improved the crystallinity of the prepared nanophosphors [14].

3.2. Optical studies

The Kubelka-Munk function, which is used as a measurement of absorption,was employed to convert the reflectance spectrum to the absorption spectrum. Fig. 4 illustrates the diffuse reflectance spectra of $Mg_{1-x}Tb_xAl_2O_4$ (x = 0.02, 0.04, 0.06, 0.08 and 0.10) nanophosphors measured in the wavelength range 200 to 500 nm.Absorbance peak in the range 200 to 300 nm is due to the band-to-band electronic transitions between filled O 2p orbitals and empty Al 3s orbitals [15, 16].The presence of absorption peaks centred around 351, 369 and 379 nm wasattributed to the transition of Tb^{3+} ions from $^7F_6$ ground state to higher excited states [17].The relation between diffuse reflectance of the sample (R_∞), absorption co-efficient (K), scattering co-efficient (s) and Kubelka- Munk function ($F(R_\infty)$) is given by [18]

$$\frac{K}{S} = \frac{(1-R_\infty)^2}{2R_\infty} = F(R_\infty) \quad (3)$$

$$F(R_\infty)h\upsilon\alpha\ (h\upsilon - E_g)^n \quad (4)$$

Here, hυ is the incident photon energy. The value of n depends on the type of optical transition and is taken as 2 for direct band gap materials such as $MgAl_2O_4$. Energy band gap values were determined by plotting the square of the Kubelka-Munk function multiplied by the photon energy against photon energy, and by extrapolating the linear portion of the curve to the horizontal energy axis [18], as illustrated in the Fig. 5. Optical energy values were found to increase with increase in Tb^{3+} ion concentration. As the crystallite size decreases with increase in Tb^{3+} ion concentration, confinement of electrons in the nanoscale cause valence band and conduction band to shift to more positive and negative side [19,20].

The FTIR spectra of $Mg_{1-x}Tb_xAl_2O_4$ (x = 0.02, 0.04, 0.06, 0.08 and 0.10) nanophosphors is depicted in Fig. 6.The figure illustrates various functional groups due to vibrations present in the synthesized phosphors. The presence of two fingerprint bands around 486 and 664 $cm^{-1}$was attributed to the stretching vibrations of AlO_6 octahedral groups and Mg-O in $MgAl_2O_4$ [21, 22]. These two bands ensured the formation of the $MgAl_2O_4$ cubic spinel system. No additional phases were observed in the FTIR spectra, which is consistent with the XRD results.

3.3. Photoluminescence studies

Fig. 7. shows the photoluminescence excitation spectrum of $Mg_{1-x}Tb_xAl_2O_4$ (x = 0.02, 0.04, 0.06, 0.08 and 0.10) series of samples under 543 nm emission wavelength. Spectra consist of a broad band in the region 200 to 270 nm, and the peaking at 242 nm corresponds to the charge transfer band derived from the $4f^8 \rightarrow 4f^7\ 5d^1$ transition of Tb^{3+} ions. All the samples exhibited several other peaks which are also similar centred at 304, 381, 339, 351, 369 and 379 nm corresponding to the transitions $^7F_6$ - $^5H_6$, $^7F_6$ - $^5H_7$, $^7F_6$ – $^5L_{7,8}$, $^7F_6$ – $^5L_9$, $^7F_6$ – $^5L_{10}$ and $^7F_6$ –

$^5D_3$, $^5G_6$ respectively [6,23,24].The excitation peak intensity is optimised at the doping concentration of x= 0.04 for Tb^{3+} doped samples. The highest peak intensity obtained at 379 nm is well matched with the excitation wavelength of commercial near-UV chips, indicating the application of prepared nanophosphors in white light emitting diodes.

The emission spectrum of $Mg_{1-x}Tb_xAl_2O_4$ (x = 0.02, 0.04, 0.06, 0.08 and 0.10) nanophosphors monitored at 379 nm excitation is shown in Fig. 8, which contains several peaks in the region 400 to 700 nm. Emission peaks at 417, 425 and 451 nm may be very well assigned to $^5D_3 \rightarrow {}^7F_{(J=5,\ 4,\ 3)}$ transitions and the peaks at 489, 543, 588 and 622 nm may be assigned to $^5D_4 \rightarrow {}^7F_{(J=6,\ 5,\ 4,\ 3)}$ transitions respectively.$^5D_3 \rightarrow {}^7F_{(J=5,\ 4,\ 3)}$ transitions are considered as blue region spectra and $^5D_4 \rightarrow {}^7F_{(J=6,\ 5,\ 4,\ 3)}$ transitions are considered as green region spectra [24, 25].The intensity of $^5D_3 \rightarrow {}^7F_{(J=5,\ 4,\ 3)}$ transitions was lower than $^5D_4 \rightarrow {}^7F_{(J=6,\ 5,\ 4,\ 3)}$ transitions, due to cross-relaxation among Tb^{3+}ions [26] which can be expressed by the equation as

$$Tb^{3+}(^5D_3) + Tb^{3+}(^7F_6) \rightarrow Tb^{3+}(^5D_4) + Tb^{3+}(^7F_0) \quad (5)$$

Electrons in the $^5D_3$ state got de-excited to $^5D_4$ state and the $^7F_6$ electrons got excited to $^7F_0$ state, due to which weakening of $^5D_3 \rightarrow {}^7F_{(J=5,\ 4,\ 3)}$ transitions and strengthening of $^5D_4 \rightarrow {}^7F_{(J=6,\ 5,\ 4,\ 3)}$ transitions occurred.The most intense emission was at 543 nm corresponding to $^5D_4 \rightarrow {}^7F_5$ transition. Photoluminescence emission intensity varied with Tb^{3+} ion concentration and the intensity was found to be maximum for the doping concentration of x= 0.04. On further increasing the concentration of doping ions, the intensity was found to decrease due to the enhancement of non-radiative transitions [26, 27].The variation of $^5D_3 \rightarrow {}^7F_4$transition and $^5D_4 \rightarrow {}^7F_5$ with Tb^{3+} ion concentration is shown in Fig. 9.The different excitation and emission transitions of trivalent terbium ions are displayed in Fig. 10.

The concentration quenching effect at higher concentrations of Tb^{3+} ions can be understood by Dexter's energy transfer mechanism. The two types of energy transfer that can occur between neighbouring activator ions are exchange interaction and multipolar interaction. The critical distance for energy transfer was estimated using the Blasse equation [24,27] given as

$$R = 2\left(\frac{3V}{4\Pi XN}\right)^{\frac{1}{3}} \quad (6)$$

where X denotes the optimum concentration of Tb^{3+} ions, V represents the unit cell volume and N, the number of available crystallographic sites occupied by the activator ions in the $MgAl_2O_4$ unit cell, which is equal to 8. For the critical concentration x=0.04, the estimated R value is greater than 5 Å, confirming that phonon-assisted multipole-multipole interaction is the mechanism behind the energy transfer process in the synthesized nanophosphors [28,29]. According to Dexter's theory, the types of mechanisms involved in the multipolar interactions are dipole-dipole, dipole-quadrupole and quadrupole-quadrupole interactions. The phenomenon of concentration quenching was explained by the relation between the intensity of emission (I) per activator ion and activator ion concentration (x), proposed by Van Uitert as [30,31]

$$\log\left(\frac{I}{X}\right) = f - \left(\frac{s}{3}\right)\log X \quad (7)$$

where f = log K–logβ,ands takes the values 6, 8 and 10 for dipole-dipole, dipole-quadrupole and quadrupole-quadrupole interactions, respectively. Log X was plotted against log [I/X] [Fig. 11] and using the linear fit, the slope obtained was -1.98 and the estimated value of 's' is 5.94. This is closer to the theoretical value of 6, which concludes that dipole-dipole interaction is responsible for concentration quenching in $Mg_{1-x}Tb_xAl_2O_4$ (x = 0.02, 0.04, 0.06, 0.08 and 0.10) nanophosphors [32–34].

To understand more about the phenomenon of concentration quenching, luminescence decay kinetic curves for $Mg_{1-x}Tb_xAl_2O_4$ (x = 0.02, 0.04, 0.06, 0.08 and 0.10) nanophosphors corresponding to $^5D_4 \rightarrow {}^7F_5$ transition (543 nm) emission at 379 nm excitation wavelength were monitored, and are presented in Fig. 12. The decay curve is perfectly fitted through double exponential function, given by the equation

$$I(t) = A_1 \exp\left(\frac{-t}{\tau_1}\right) + A_2 \exp\left(\frac{-t}{\tau_2}\right) \quad (8)$$

where A_1 and A_2 are fitting parameters, $\tau_1$andτ_2 are exponential components of decay lifetimes and $I(t)$ is the intensity of emission at time t.The average lifetime values (τ_{avg}) of the synthesized phosphors were calculated using the equation [35,36]

$$\tau_{avg} = \frac{A_1\tau_1^2 + A_2\tau_2^2}{A_1\tau_1 + A_2\tau_2} \quad (9)$$

Decrease in luminescent decay time values was observed with increase in Tb^{3+} ion concentration, indicating that the lifetime values are concentration dependent.The observed decrease in the lifetime values from 1.8274 to 1.6120 ms with increase in Tb^{3+} ion concentration from x=0.02 to x=0.10 was mainly due to the increase in non-radiative transition rate. As the concentration of doping ions increases, the ions move closer to one another resulting in the quick transfer of energy, providing a different decay path leading to a reduced lifetime.

CIE 1931 chromaticity diagram is used to identify the exact colour emission of the prepared nanophosphors. The CIE co-ordinates of all samples are almost the same and are located in the green area as represented in the CIE diagram [Fig. 13]. Correlated colour temperature is calculated using the McCamy relation, given by

$$CCT = -437m^3 + 3601m^2 - 6861m + 5514.31 \quad (10)$$

where m= $(x-x_e)/(y_e-y)$ represents the inverse slope line and (x_e = 0.3320, y_e = 0.1858) indicates the chromaticity epicentre [24].The colour purity of the prepared samples was determined using [24, 37]

$$\text{Colour purity} = \frac{\sqrt{(x-x_i)^2+(y-y_i)^2}}{\sqrt{(x_d-x_i)^2+(y_d-y_i)^2}} \times 100\ \% \quad (11)$$

where (x_d, y_d), (x, y) and (x_i, y_i) are the chromaticity coordinates of the dominant wavelength, emission light and coordinates of white light in the CIE diagram (x_i=0.3333, y_i = 0.3333), respectively. Table 1 lists the obtained chromaticity co-ordinates, CCT values and colour purity values obtained from the emission spectra of $Mg_{1-x}Tb_xAl_2O_4$ (x = 0.02, 0.04, 0.06, 0.08 and 0.10) nanophosphors calculated by CIE colour matching functions. All the prepared

nanophosphors exhibit the CCT values between 5000 and 9000 K demonstrating that $Mg_{1-x}Tb_xAl_2O_4$ (x = 0.02, 0.04, 0.06, 0.08 and 0.10) nanophosphors play an important role in UV-excited white LED's.

Conclusions

Pure singlephase $Mg_{1-x}Tb_xAl_2O_4$ (x = 0.02, 0.04, 0.06, 0.08 and 0.10) nanophosphors were synthesized via polyvinylpyrrolidone (PVP) polymer capped citrate nitrate sol-gel method. X-ray diffraction results confirmed the formation of cubic spinel structured nanocrystalline $MgAl_2O_4$. The crystallite size varied significantly with changes in Tb^{3+} ion concentration, indicating that the doping influences the structural parameters of the prepared nanophosphors.The TEM images confirm the formation of spherically morphological particles with very little agglomeration.Hence, the XRD and TEM results reveal that PVP acted as surface capping and stabilizing agent during the formation of $Mg_{1-x}Tb_xAl_2O_4$ (x = 0.02, 0.04, 0.06, 0.08 and 0.10) nanophosphors. The optical band gaps of the prepared nanophosphors were calculated using the UV visible diffuse reflectance spectra via the Kubelka-Munk relation. The estimated band gap values were found to increase with increase in the concentration of Tb^{3+} ions, which may be due to confinement of electrons in the nanoscale. FTIR spectra displayed various functional groups present in the samples corresponding to the cubic spinel structured $MgAl_2O_4$. Under excitation at 379 nm, the emission spectra of the synthesized nanophosphors show both blue and green corresponding to the transitions $^5D_3 \rightarrow {}^7F_{(J=5,\ 4,\ 3)}$ and $^5D_4 \rightarrow {}^7F_{(J=6,\ 5,\ 4,\ 3)}$, among which $^5D_4 \rightarrow {}^7F_5$ transition at 543 nm is the most intense.Dexter's theory helps in explaining the concentration quenching mechanism that occurred after the optimum concentration of $Mg_{0.96}Tb_{0.04}Al_2O_4$.The dipole-dipole interaction is accountable for the quenching phenomenon in $Mg_{1-x}Tb_xAl_2O_4$ (x = 0.02, 0.04, 0.06, 0.08 and 0.10) nanophosphors. Luminescence decay curves indicated a decrease in lifetime values, which was attributed to the increase in non-radiative transition rate. The colour purity and correlated colour temperature (CCT) of the prepared nanophosphors were evaluated from the CIE co-ordinates. The evaluated structural and optical characteristics suggest that $Mg_{1-x}Tb_xAl_2O_4$ (x = 0.02, 0.04, 0.06, 0.08 and 0.10) nanophosphors are promising materials in the green region and have excellent practical applications in optoelectronics, especially in white LEDs.

Introduction

1. P. A. Tanner, 183 (2010).

2. B. Baruah and R. Sarkar, InterCeram Int. Ceram. Rev. **69**, 40 (2020).

3. M. Y. Nassar, I. S. Ahmed, and I. Samir, Spectrochim. Acta - Part A Mol. Biomol. Spectrosc. **131**, 329 (2014).

4. I. E. Kolesnikov, E. V. Golyeva, A. V. Kurochkin, and M. D. Mikhailov, J. Alloys Compd. **654**, 32 (2016).

5. I. Ganesh, Int. Mater. Rev. **58**, 63 (2013).

6. D. Valiev, O. Khasanov, E. Dvilis, S. Stepanov, V. Paygin, and A. Ilela, Phys. Status Solidi Basic Res. **257**, 2 (2020).

7. C. Parthasaradhi Reddy, V. Naresh, R. Ramaraghavulu, B. H. Rudramadevi, K. T. Ramakrishna Reddy, and S. Buddhudu, Spectrochim. Acta - Part A Mol. Biomol. Spectrosc. **144**, 68 (2015).

8. K. M. Koczkur, S. Mourdikoudis, L. Polavarapu, and S. E. Skrabalak, Dalt. Trans. **44**, 17883 (2015).

9. H. Shao, Y. Huang, H. S. Lee, Y. J. Suh, and C. O. Kim, Curr. Appl. Phys. **6**, 195 (2006).

10. H. Dahiya, M. Dalal, J. Dalal, V. B. Taxak, S. P. Khatkar, and D. Kumar, Mater. Res. Bull. **99**, 86 (2018).

11. R. J. Wiglusz and T. Grzyb, Opt. Mater. (Amst). **33**, 1506 (2011).

12. S. J. Hong and A. V. Virkar, J. Am. Ceram. Soc. **78**, 433 (1995).

13. P. Ayyub, V. R. Palkar, S. Chattopadhyay, and M. Multani, Phys. Rev. B **51**, 6135 (1995).

14. R. Zein, I. Alghoraibi, C. Soukkarieh, M. T. Ismail, and A. Alahmad, Micromachines **13**, (2022).

15. K. V. Kumar and S. D. Bhavani, East Eur. J. Phys. **2023**, 355 (2023).

16. S. Sameera, V. Vidyadharan, S. Sasidharan, and K. G. Gopchandran, J. Sci. Adv. Mater. Devices **4**, 524 (2019).

17. R. K. Verma, K. Kumar, and S. B. Rai, Solid State Sci. **12**, 1146 (2010).

18. R. G. Abhilash Kumar, S. Hata, and K. G. Gopchandran, J. Lumin. **263**, 120150 (2023).

19. A. A. Dakhel, Mater. Res. **19**, 379 (2016).

20. M. Dutta, J. M. Kalita, and G. Wary, Optik (Stuttg). **240**, 166946 (2021).

21. S. Tripathy and D. Bhattacharya, J. Asian Ceram. Soc. **1**, 328 (2013).

22. V. Singh, Ravita, S. Kaur, A. S. Rao, and H. Jeong, Optik (Stuttg). **244**, 167323 (2021).

23. D. Y. Medina-Velazquez, U. Caldiño, A. Morales-Ramirez, J. Reyes-Miranda, R. E. Lopez, R. Escudero, R. Ruiz-Guerrero, and M. F. Morales Perez, Opt. Mater. (Amst). **87**, 3 (2019).

24. P. Kumar, D. Singh, I. Gupta, S. Singh, S. Nehra, and R. Kumar, RSC Adv. **13**, 7752 (2023).

25. B. Zheng, J. Hong, B. Chen, Y. Chen, R. Lin, C. Huang, C. Zhang, J. Wang, L. Lin, and Z. Zheng, Results Phys. **28**, 104595 (2021).

26. S. Devi, A. Khatkar, V. B. Taxak, A. Hooda, P. Sehrawat, S. Singh, and S. P. Khatkar, J. Lumin. **221**, 117064 (2020).

27. J. Young Park, H. Chae Jung, G. Seeta Rama Raju, B. Kee Moon, J. H. Jeong, and J. Hwan Kim, J. Lumin. **130**, 478 (2010).

28. A. Manuscript, J. Chem. Soc. Dalt. Trans. 1772 (1972).

29. K. Rawat, A. K. Vishwakarma, and K. Jha, Mater. Res. Bull. **124**, 110750 (2020).

30. A. Fernández-Osorio, C. E. Rivera, A. Vázquez-Olmos, and J. Chávez, Dye. Pigment. **119**, 22 (2015).

31. Neharika, V. Kumar, J. Sharma, V. K. Singh, O. M. Ntwaeaborwa, and H. C. Swart, J. Electron Spectros. Relat. Phenomena **206**, 52 (2016).

32. M. Peng, X. Yin, P. A. Tanner, C. Liang, P. Li, Q. Zhang, and J. Qiu, J. Am. Ceram. Soc. **96**, 2870 (2013).

33. Q. Tang, T. Yang, B. Guo, B. Peng, H. Huang, and J. Ao, Optik (Stuttg). **224**, 165770 (2020).

34. L. G. Van Uitert, J. Electrochem. Soc. **114**, 1048 (1967).

35. E. Erdoğmuş and E. Korkmaz, Optik (Stuttg). **125**, 4098 (2014).

36. A. Dhahri, K. Horchani-Naifer, A. Benedetti, F. Enrichi, M. Férid, and P. Riello, Opt. Mater. (Amst). **35**, 1184 (2013).

37. M. Venkataravanappa, H. Nagabhushana, B. Daruka Prasad, G. P. Darshan, R. B. Basavaraj, and G. R. Vijayakumar, Ultrason. Sonochem. **34**, 803 (2017).

Table. 1. The obtained chromaticity co-ordinates, CCT values and colour purity values of $Mg_{1-x}Tb_xAl_2O_4$ (x = 0.02, 0.04, 0.06, 0.08 and 0.10) nanophosphors.

$Mg_{1-x}Tb_xAl_2O_4$	**x=0.02**	**x=0.04**	**x=0.06**	**x=0.08**	**x=0.10**
x	0.3072	0.3134	0.3105	0.3112	0.3109
y	0.5445	0.5780	0.5935	0.5750	0.5428
CCT (K)	6009	5852	5890	5895	5936
Colour purity (%)	59.05	74.27	72.47	67.34	58.46

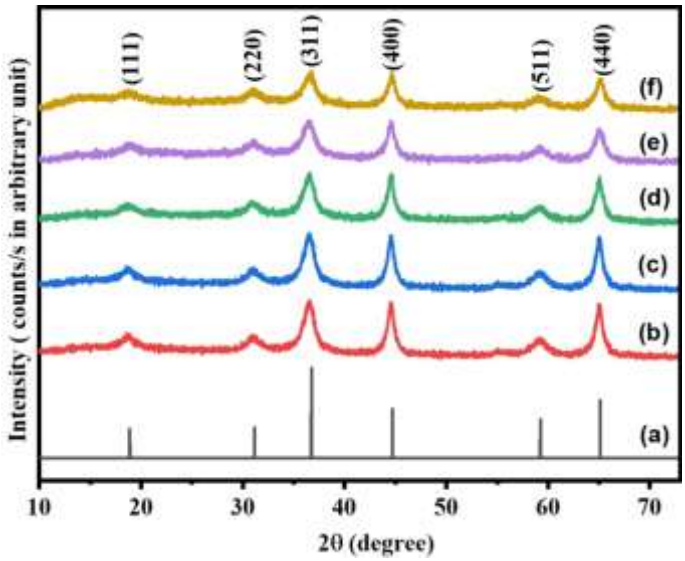

Fig.1. X-ray diffraction patterns: (a) $MgAl_2O_4$ standard data: $Mg_{1-x}Tb_xAl_2O_4$ nanophosphors with different Tb^{3+} concentration (x) (b) 0.02 (c) 0.04 (d) 0.06 (e) 0.08 (f) 0.1.

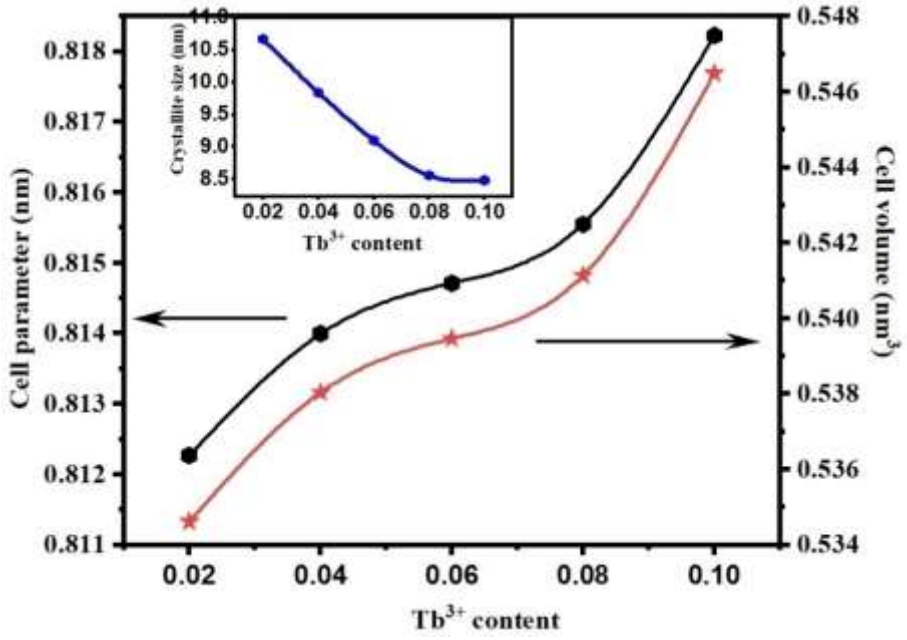

Fig. 2. Variation of cell parameter and cell volume of $Mg_{1-x}Tb_xAl_2O_4$ nanophosphors with different Tb^{3+} concentration (x) (b) 0.02 (c) 0.04 (d) 0.06 (e) 0.08 (f) 0.1

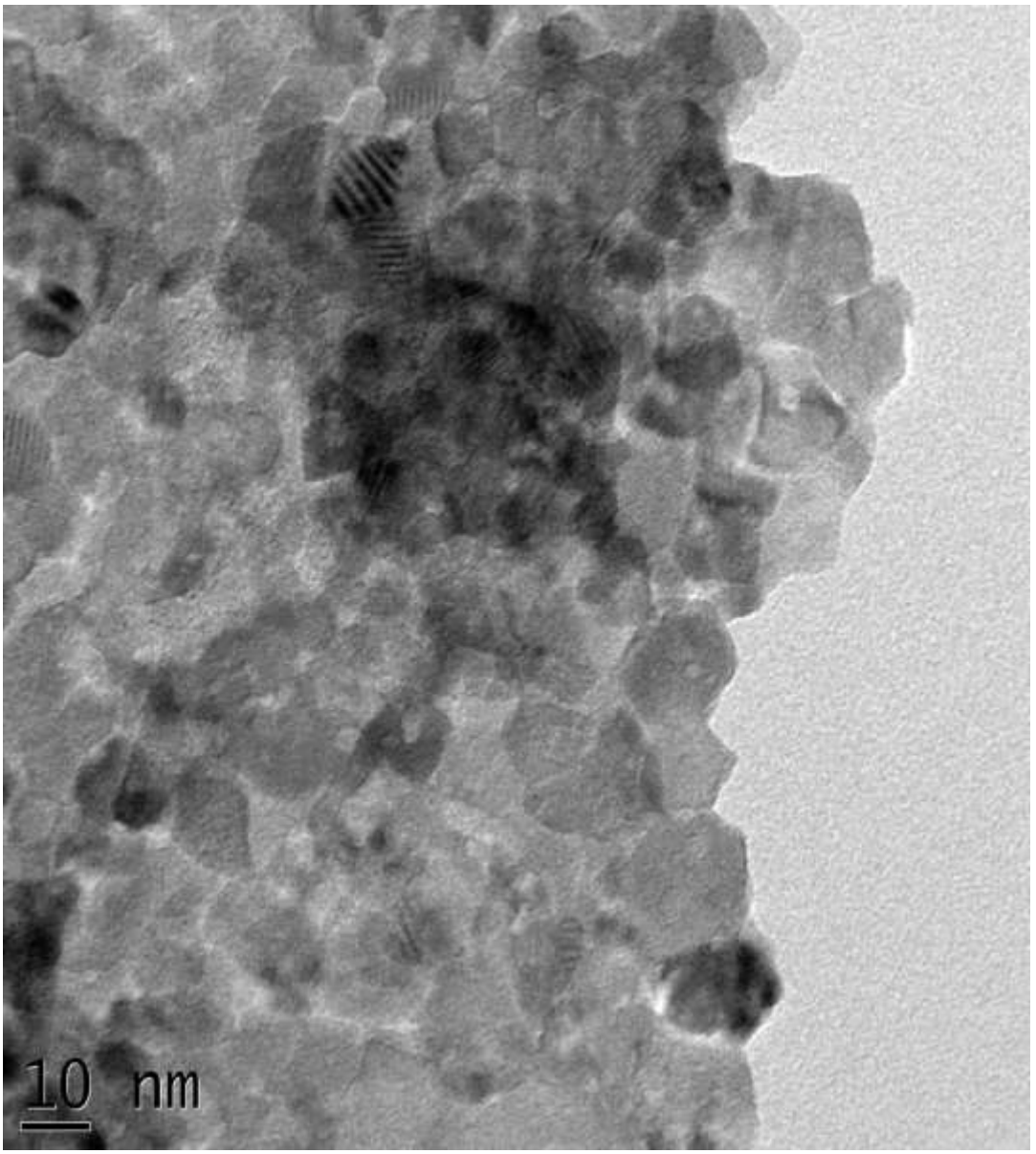

Fig.3. High resolution TEM image of $Mg_{0.96}Tb_{0.04}Al_2O_4$ nanophosphor.

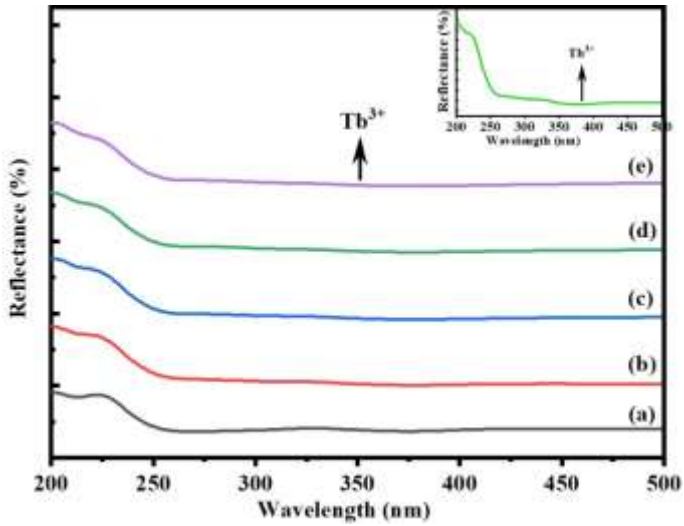

Fig.4. Diffuse reflectance spectra of $Mg_{1-x}Tb_xAl_2O_4$ nanophosphors with different Tb^{3+} concentration (x) (a) 0.02 (b) 0.04 (c) 0.06 (d) 0.08 (e) 0.1. (inset shows the diffuse reflectance spectrum of $Mg_{0.96}Tb_{0.04}Al_2O_4$ nanophosphor).

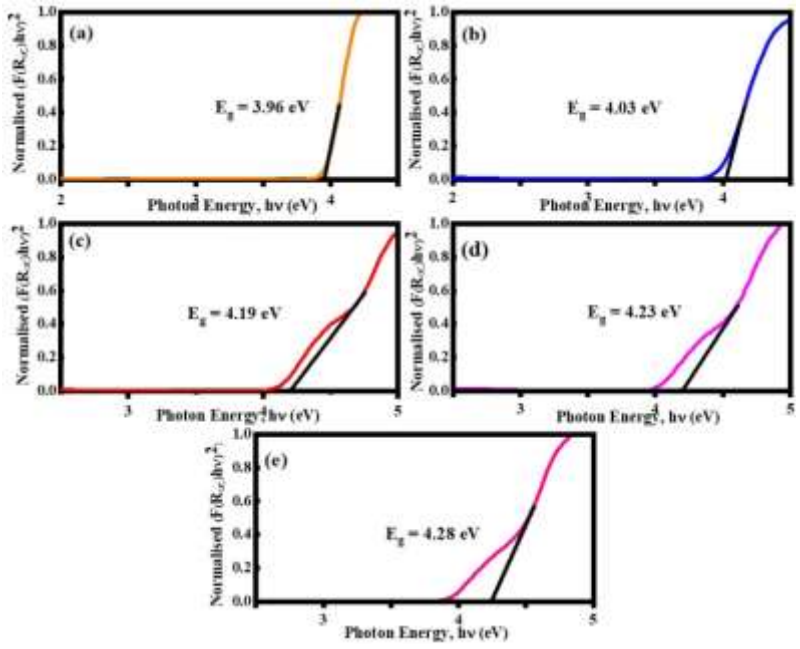

Fig.5. Kubelka-Munk plots of $Mg_{1-x}Tb_xAl_2O_4$ nanophosphors with different Tb^{3+} concentration (x) (a) 0.02 (b) 0.04 (c) 0.06 (d) 0.08 (e) 0.1.

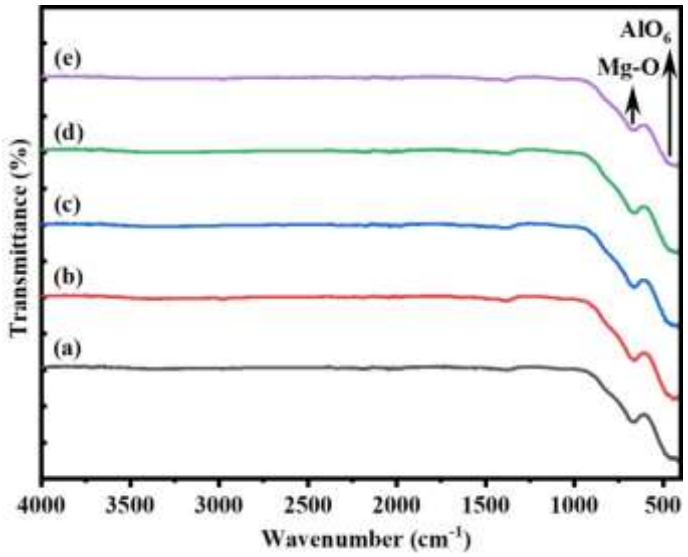

Fig.6. FTIR spectra of $Mg_{1-x}Tb_xAl_2O_4$ nanophosphors with different Tb^{3+} concentration (x) (a) 0.02 (b) 0.04 (c) 0.06 (d) 0.08 (e) 0.1.

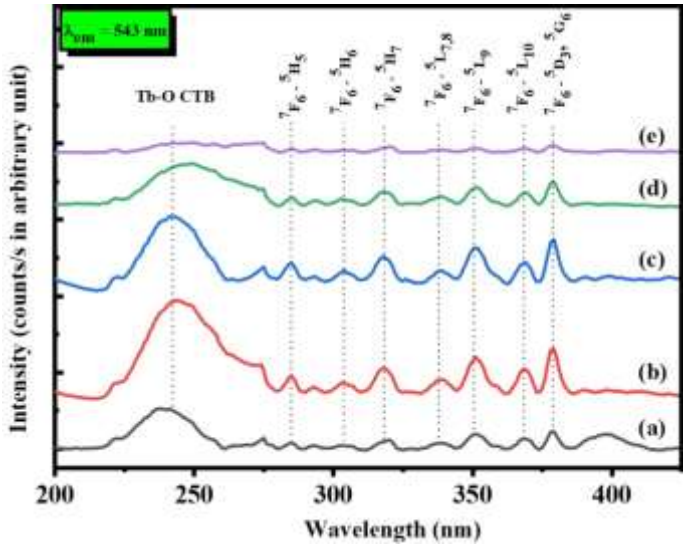

Fig.7. Excitation spectra of $Mg_{1-x}Tb_xAl_2O_4$ nanophosphors with different Tb^{3+} concentration (x) (a) 0.02 (b) 0.04 (c) 0.06 (d) 0.08 (e) 0.1.

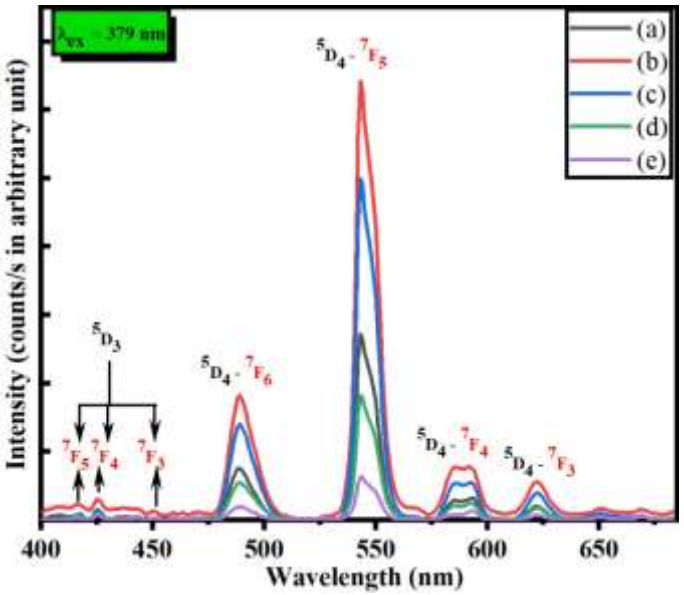

Fig.8. Emission spectra of $Mg_{1-x}Tb_xAl_2O_4$ nanophosphors with different Tb^{3+} concentration (x) (a) 0.02 (b) 0.04 (c) 0.06 (d) 0.08 (e) 0.1.

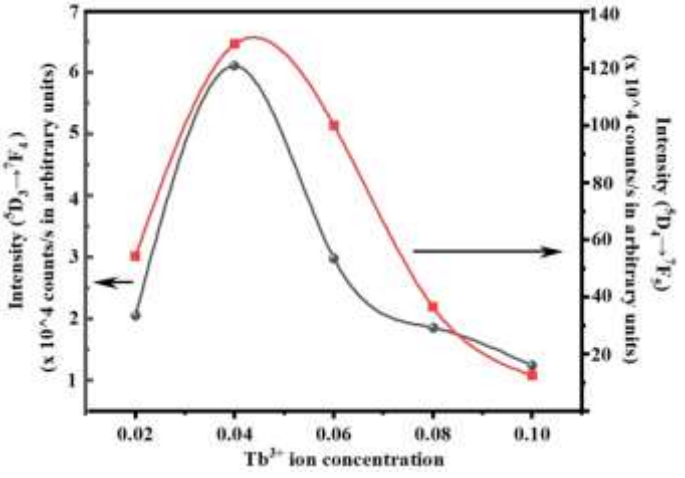

Fig.9. Dependence of emission intensity of $^5D_3 \rightarrow ^7F_4$ transition and $^5D_4 \rightarrow ^7F_5$ transition of $Mg_{1-x}Tb_xAl_2O_4$ nanophosphors with different Tb^{3+} concentration (x= 0.02. 0.04, 0.06, 0.08 and 0.1)

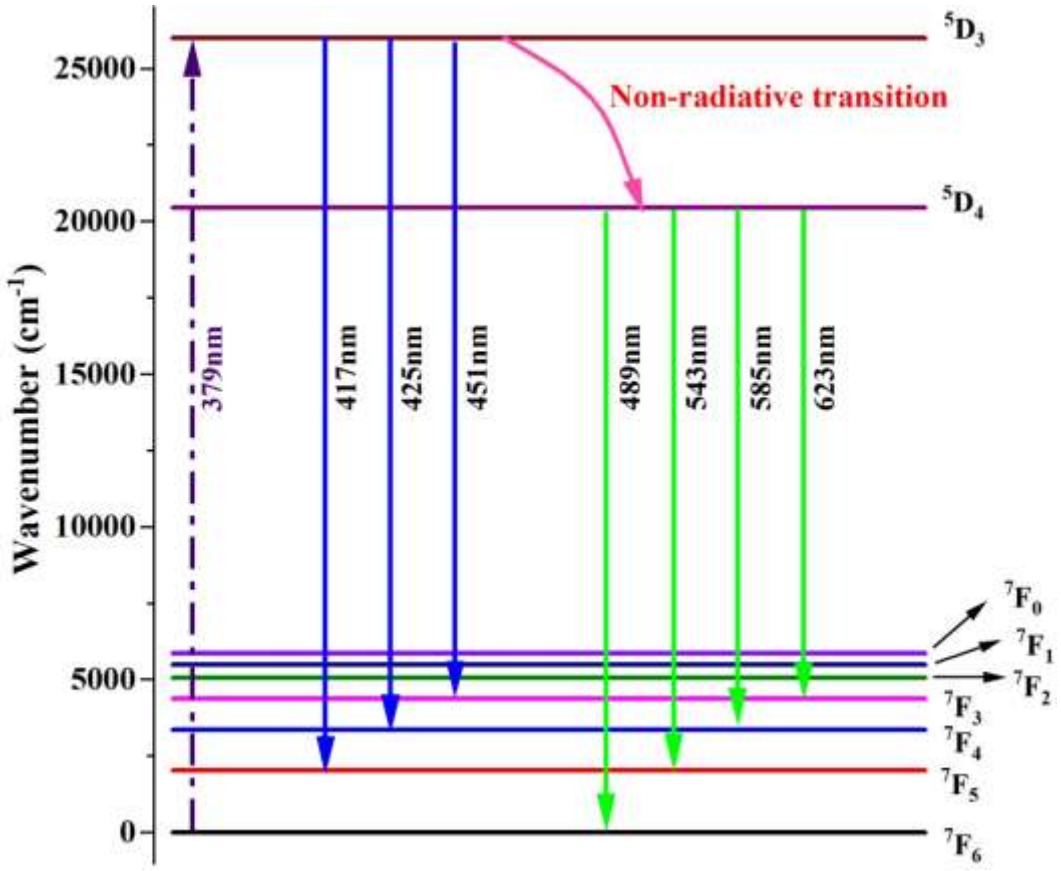

Fig.10. The different excitation and emission transitions of trivalent terbium ions.

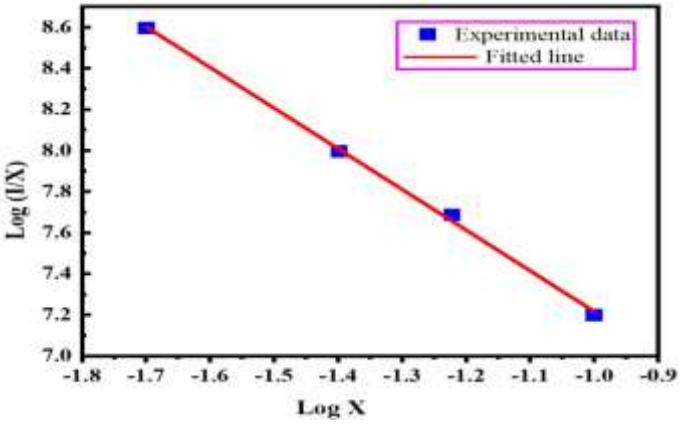

Fig. 11. Plot of log (I/X) vs. log (X) of Tb^{3+} ions in $Mg_{1-x}Tb_xAl_2O_4$ nanophosphors.

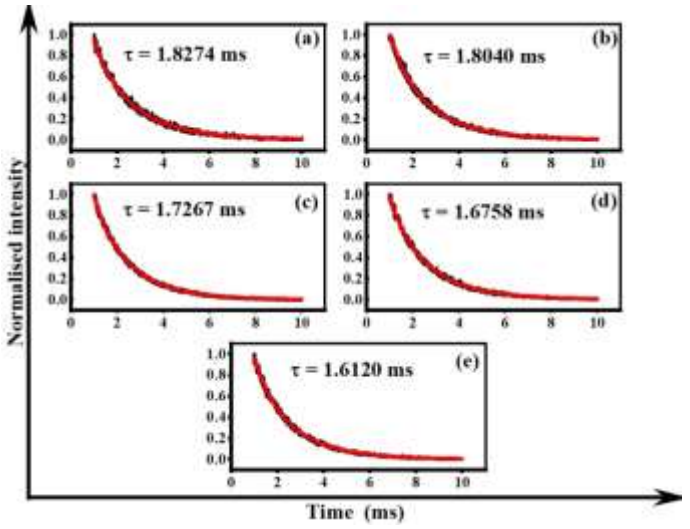

Fig.12. Luminescent decay curves of $Mg_{1-x}Tb_xAl_2O_4$ nanophosphors with different Tb^{3+} concentration (x) (a) 0.02 (b) 0.04 (c) 0.06 (d) 0.08 (e) 0.1

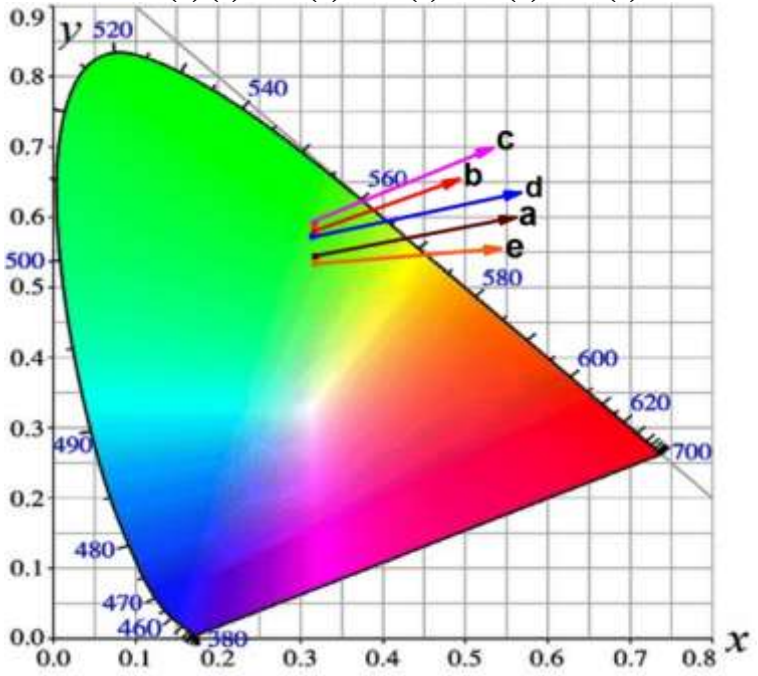

Fig. 13. The CIE chromaticity diagram of $Mg_{1-x}Tb_xAl_2O_4$ nanophosphors with different Tb^{3+} concentration (x) (a) 0.02 (b) 0.04 (c) 0.06 (d) 0.08 (e) 0.1